Journal of The Electrochemical Society, **161** (8) E3086-E3096 (2014)
0013-4651/2014/161(8)/E3086/11/$31.00 © The Electrochemical Society

JES Focus Issue on Mathematical Modeling of Electrochemical Systems at Multiple Scales

A Surrogate-Based Multi-Scale Model for Mass Transport and Electrochemical Kinetics in Lithium-Ion Battery Electrodes

Wenbo Du,[a,z] Nansi Xue,[a,*] Wei Shyy,[b] and Joaquim R. R. A. Martins[a]

[a]*Department of Aerospace Engineering, University of Michigan, Ann Arbor, Michigan 48109, USA*
[b]*Department of Mechanical Engineering, Hong Kong University of Science and Technology, Clear Water Bay, Hong Kong*

Lithium-ion batteries are now used in a wide range of applications, and much knowledge has been accumulated in the relevant physical phenomena. However, the application of this knowledge in battery design still relies on an inefficient manual process, in large part due to limitations in existing computational models. To address this, a multi-scale model is developed that incorporates microscopic simulation data for effective ion diffusivity and electronic conductivity, and interfacial electrochemical kinetics, into a macroscopic homogeneous model at the cell scale. Microscopic physics-based models are applied to 3D microstructures, and automated simulations are performed for statistically significant averaging of the results. A surrogate model couples the length scales by precomputing solutions based on a design of experiments. Results for the porosity-tortuosity relationship are compared to experimental data in the literature, and global sensitivity analysis is performed to quantify the relative impact of ion concentration and electric potential distribution on the electrochemical kinetics profile. The resulting multi-scale model successfully reproduces the microscopic solution while retaining the computational efficiency of the macroscopic homogeneous model. These attributes make it a suitable candidate for implementation in an automated simulation and optimization framework that may lead to a more efficient design process for high performance batteries.

Manuscript submitted February 6, 2014; revised manuscript received March 17, 2014. Published April 11, 2014. *This paper is part of the JES Focus Issue on Mathematical Modeling of Electrochemical Systems at Multiple Scales*.

Lithium-ion batteries have attracted considerable interest in recent years due to their high energy and power density compared to other battery technologies, which make them suitable for high performance applications such as portable electronic devices.[1] Their successful deployment in electric vehicles also has significant implications to the transportation sector, especially in light of environmental concerns linked to carbon emissions. These considerations, in conjunction with advances in key areas such as electrochemistry and materials science, has fostered substantial progress in understanding the relevant physical phenomena that occur within battery cells. However, the application of this knowledge in the design and manufacture of battery cells and packs has not been fully realized, primarily due to a limitation in the use of sophisticated modeling and optimization techniques. In practice, battery design still relies on ad-hoc decisions in areas where existing models provide inadequate information about battery behavior and performance, resulting in a lengthy and inefficient design process that does not necessarily lead to an optimal final design. Therefore, there exists a critical need to establish advanced computational models capable of efficiently modeling battery behavior. Such models would enable a greater degree of automation in the design process, while also achieving improved energy and power performance.

Much progress has been made in the modeling and analysis of lithium-ion cells and electrodes, including the use of numerical optimization tools for electrode design optimization.[2-5] Specialized models such as single-particle models,[6,7] capacity fade models,[8] and microscopic models,[9] are very useful for investigating the relevant physics within battery electrodes. However, they are of limited use to design, as they focus on localized phenomena without consideration of cell-level behavior. Three-dimensional models avoid this limitation, but are prohibitively expensive for sensitivity analysis and optimization purposes unless confined to small cross sections with significant uncertainty in microstructure.[10] In contrast, equivalent circuit models [11,12] are computationally inexpensive, but their overly simplified treatment of battery physics makes them unsuitable for design purposes, and their applicability is limited to simple control systems. More detailed system-level analysis and control, however, requires more sophisticated models that demand greater computational resources.[13]

One of the most successful models for design is the pseudo-2D model based on porous electrode and concentrated solution theory.[14,15] This computationally efficient model has been successfully applied in a variety of studies, including analysis of stress generation[16] and cell design.[17,18] Reformulated versions of the pseudo-2D model are especially well suited for design optimization due to their improved computational efficiency.[19,20] However, one shortcoming of these models is that certain closure terms in the governing equations, such as the effective transport coefficients and volumetric reaction current density, are based on homogenization. This means that approximations are made for these parameters by assuming a homogeneous medium within the electrodes, and the detailed microstructure is not considered. Experimental measurements[21] and microscopic simulations[22,23] have demonstrated that the effective diffusivity and conductivity can deviate considerably from their homogenized approximations, underscoring the need for higher fidelity models to address this discrepancy. Similarly, the electrochemical reaction rate at the solid-liquid interface has been found to vary significantly with the local microstructure.[24] Note that the purpose of pointing out the limitations of previous modeling developments is not to understate their impact, as they have all made valuable contributions toward the ultimate objective of understanding how to design better batteries. Instead, these examples serve to illustrate the specific attributes that are missing from existing models, and to highlight the key advantages of the method presented in this article.

A more accurate treatment of the aforementioned microstructural properties can be achieved through detailed 3D multiphysics simulations conducted on sample microstructures. The resulting simulation data can then be incorporated into existing cell models, such as the pseudo-2D model, by coupling the necessary state variables to produce a multi-scale model. Such an approach allows important effects of microstructural geometry on multiphysics phenomena to be considered in cell-level analysis and design. The concept of models that couple sub-models to simulate physical processes occurring simultaneously at multiple length scales is not new. These modeling approaches have been utilized in a variety of engineering systems, including lithium-ion batteries.[25] Some notable examples include models analyzing the impact of external pressure[26] and intercalation-induced stress on separators[27] and porous electrodes.[28] The latter model has also been incorporated into an adjoint sensitivity analysis framework for design optimization.[29] A common attribute of

*Electrochemical Society Student Member.
zE-mail: wenbodu@umich.edu

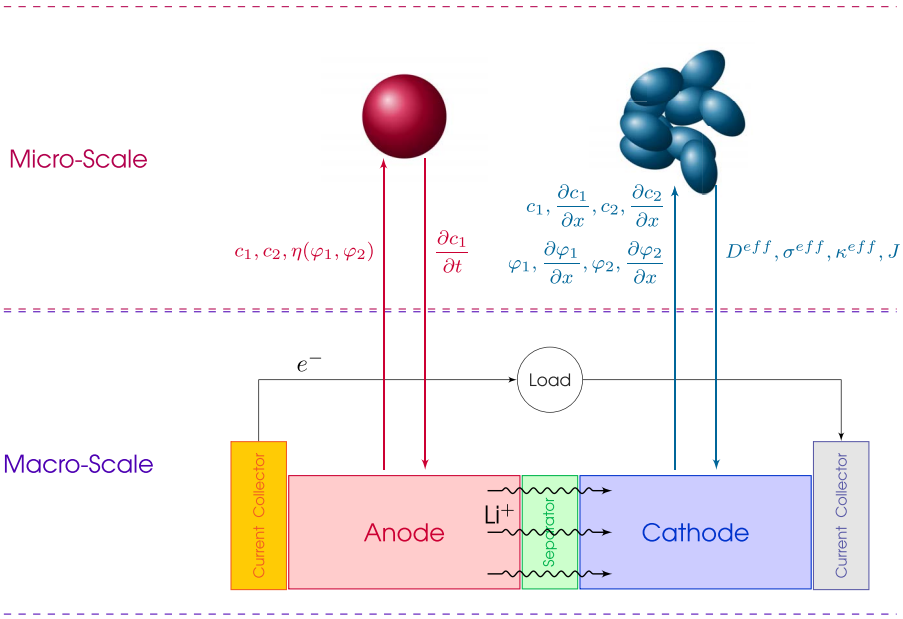

Figure 1. Macroscopic and microscopic scale models, with multi-scale coupling variables shown.

such models is that they involve explicit coupling of the governing equations at multiple length scales, meaning that all sets of equations are solved simultaneously and bridged via a coupling interface. While such multi-scale approaches retain high fidelity in the resulting model, the computational cost can also increase significantly due to the additional governing equations that must be solved.

An optimization framework for improving the design of batteries and cells should be capable of systematically handling a large number of design variables and constraints, given the complexity of the battery system. It is thus critically important that the computational expense of each simulation is minimized, in order to accommodate a large number of optimization iterations. For this reason, we select the surrogate modeling approach to couple the macroscopic (electrode) and microscopic (particle) length scales. This method differs from those in other multi-scale models in that the state variables of the length scales are not coupled explicitly, but rather implicitly via surrogate functions constructed from pre-computed simulation data based on a design of experiments. Since they are analytically defined, the computational cost of evaluating a surrogate function is negligible compared to the cost of solving the governing equations for the microscopic scale model.[30] The resulting multi-scale model has approximately the same computational cost as the macroscopic homogeneous model, making it feasible for cell optimization and design. The difficulties of applying this method include quantifying the error due to uncertainty in fitting the surrogate model, and the numerical robustness of the coupling interface.

The macroscopic scale is described by the pseudo-2D homogeneous porous electrode model, which accounts for transient diffusion and conduction of ions and electrons in the multiphase porous electrodes, as well as ion diffusion within spherical particles.[14] The microscopic scale model makes use of the concept of a Representative Elementary Volume (REV), which represents a part of a 3D electrode microstructure as a cluster of particles. Here, the REV are sometimes referred to as "realizations" of the microstructure generation algorithm. In this multi-scale model, we focus our efforts on the cathode, while recognizing a similar deficiency in accurate modeling of the anode microstructure. Given the need for better computational tools for designing improved batteries, and the advantages and challenges of the selected multi-scale modeling approach, we define the following objectives in this work:

1. Establish a robust process for automating a large number of microscopic scale 3D multiphysics simulations for the effective transport coefficients and volumetric reaction current density in electrode microstructures;
2. Construct surrogate models from the microscopic simulation data using a design of experiments, and quantify the uncertainty in the models using cross-validation methods;
3. Perform global sensitivity analysis to compare the relative impact of multiple parameters and reduce or refine the parameter space if possible;
4. Incorporate microstructural properties into the multi-scale model by bridging the two length scales using the surrogate model.

The remainder of this article is organized as follows. First, we detail the key steps to the multi-scale modeling methodology: microstructure generation and meshing, multiphysics simulations at the microscopic scale, and surrogate modeling. We then present the microscopic simulation results and demonstrate some sample cases using the completed multi-scale model. Finally, we offer a discussion of the key findings and some concluding remarks on future research directions.

Methodology

The multi-scale model of the cell is illustrated in Figure 1. During discharge, a current flows between two current collectors connected to the negative electrode (anode) and positive electrode (cathode). In order to balance the flow of electrons, positively charged lithium ions travel from the anode through a porous separator to the cathode. The anode is modeled in the same manner as existing macroscopic homogeneous models, with transient lithium ion concentration calculated in a single spherical particle at each computational node; this model is described in further detail in Appendix A. In contrast, microscopic simulations are applied to microstructures in the cathode, and this multi-scale treatment involves a much larger number of coupling variables. Although it is possible to isolate the effect of the cathode by modeling a half-cell (i.e., modeling the anode as lithium foil instead of a graphite anode), we model a full cell to be consistent with our objective of creating a model suitable for cell design, and in order to obtain consistent simulation results with related work on surrogate modeling and cell optimization. The inclusion of the anode does not alter the results since it affects the multi-scale model the same as it does the homogeneous model, but it does modestly increase the overall computational cost of the multi-scale model. In this section, we present the three major aspects of the methodology: microstructure generation, governing equations for the microscopic models, and the surrogate modeling approach used to couple the two length scales.

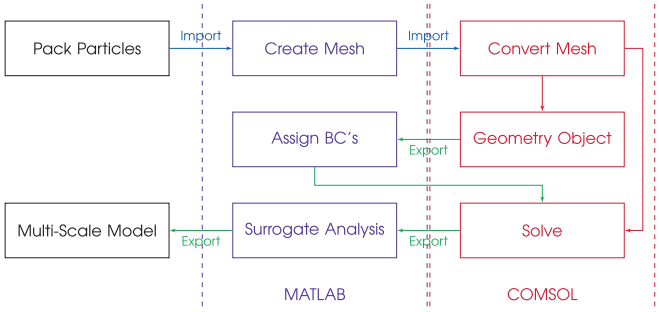

Figure 2. Numerical implementation of automated multi-scale modeling procedure.

A diagram illustrating the automated modeling and simulation process is shown in Figure 2. Since this methodology involves the use of two distinct computational environments, we make extensive use of the MATLAB-COMSOL interface to automate the process. The automation of the simulation process is essential due to the numerous importing and exporting steps that would render manual iterations impractical. Note that the processes in MATLAB are generally much less computationally expensive than the finite element analysis (FEA) in COMSOL, so the computational efficiency of the MATLAB environment is not of critical concern. Also note that while simulation parameter values are selected to roughly correspond to properties of lithium manganese oxide, the present methodology is suitable for various electrode materials whose behavior is well described by dimensionless parameters for linear diffusion and conduction.[31]

Microstructure generation and meshing.— Sample microstructures are generated based on the random packing of ellipsoidal particles. In the cases demonstrated here, a fixed number of monodisperse prolate ellipsoidal particles with $AR = 2$ are packed using an efficient molecular dynamics (MD) algorithm implemented in Fortran that contributes very little to the total computational cost of the overall methodology due to the relatively small number of particles considered.[32] Although the MD model is capable of handling polydisperse particles, we consider only monodisperse particles since reliable size and shape data for polydisperse particles are not available. The aspect ratio is selected to minimize intercalation-induced stress.[6] Three different REV sizes (10 μm, 20 μm, 40 μm) are considered here, and the number of particles is scaled with the volume of the REV (thus 10, 80, and 640 particles respectively). This approach allows an equivalent particle size of approximately 5 μm to be maintained at each REV size.

In the MD simulation, particles are randomly initialized and allowed to grow until either a specified packing density is achieved, or a jamming condition is satisfied. The resulting geometry consists of a cluster of particles that touch one another but do not overlap. Since single-phase diffusion and conduction require the solid phase of the microstructure to consist of a single contiguous object, an overlap factor of 1.1 is uniformly applied to all particles. Note that the particle size cannot be controlled exactly with this method; nonetheless, in practice a size variation of less than 10% is observed when the number of particles is fixed.

The microscopic model considers a two-phase system, where the volume occupied by the particles is modeled as active solid, and the surrounding void is modeled as liquid electrolyte. Consequently, additional phases such as binders and conductive additives are ignored, although the effects of these phases are not ignored. Instead, they are modeled via the bulk properties of the electrode materials; this is similar to their treatment in the macroscopic model. Finally, to ensure a robust method for defining boundary conditions on a large number of sample microstructures, each REV must be defined in the same cubic domain. This is accomplished by removing portions of the particle cluster protruding outside the cube. Readers interested in further details of the microstructure generation algorithm are encouraged to consult Refs. 30 and 33.

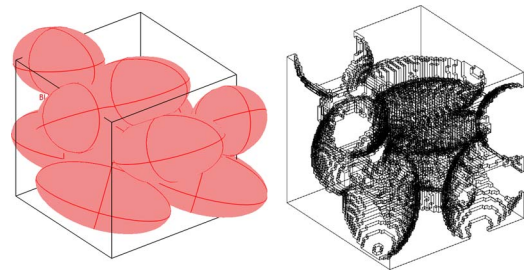

Figure 3. Packing geometry (left) and voxel mesh (right) for sample REV realization with 10 particles.

A Cartesian voxel method is implemented for all simulations, as it has been found to be suitable for microscopic FEA.[24] This method has also been previously applied to other engineering problems, such as investigation of biomechanical stress[34] and seismic ground motion.[35] As shown in Figure 3, this method creates uniformly arranged rectangular mesh elements. One advantage of the voxel method is that it is especially well suited for problems requiring a uniform mesh quality throughout the computational domain. Another important advantage is robustness, since it is able to avoid highly stretched mesh elements around sharp edges and corners (which occur frequently in clusters of ellipsoidal particles) that cause problems for other meshing techniques. A fixed mesh resolution of 0.5 μm is used for all simulations, which corresponds to a mesh size of 8.0×10^3, 6.4×10^4 and 5.1×10^5 mesh elements for the 10 μm, 20 μm and 40 μm REV cases, respectively. The same mesh resolution is applied to both solid and liquid phases, and each voxel mesh element is assigned to the phase that occupies the largest volume fraction within the voxel element. This approach produces a solid-liquid interface that allows easy implementation of boundary conditions.

Microscopic simulations.— In the macroscopic porous electrode model, the effective diffusivity and conductivity in the liquid phase are related to bulk values via the Bruggeman equation:

$$D^* \equiv \frac{\sigma^{\text{eff}}}{\sigma^{\text{bulk}}} = \frac{\kappa^{\text{eff}}}{\kappa^{\text{bulk}}} = \frac{D_2^{\text{eff}}}{D_2^{\text{bulk}}} = \varepsilon^{\alpha} \quad [1]$$

where σ and κ denote the electronic conductivity in the solid and liquid phase respectively, and D_2 is the ionic diffusivity in the liquid phase. A value of $\alpha = 1.5$, corresponding to an ideal sphere, is most commonly used. As mentioned previously, a number of studies have confirmed that the effective diffusivity and conductivity in real electrodes can vary substantially from this approximation. This is because actual diffusion and conduction depends not only on the porosity ε, but also on other parameters such as tortuosity. Accurate models for diffusion and conduction are especially important for cells containing common cathode materials like lithium manganese oxide, whose performance has been shown to be determined by the scaling of dimensionless parameters derived from electrode diffusivity and conductivity.[31] To develop a multi-scale treatment that more accurately models the ion and electron transport in electrodes, we conduct microscopic simulations on generated microstructures by solving the steady-state 3D diffusion equation:

$$\nabla \cdot (D^{\text{bulk}} \nabla \cdot c) = 0 \quad [2]$$

where the concentration c is the state variable for which the equation is solved. Since the bulk transport coefficient D^{bulk} is independent of the concentration c, this reduces to the Laplace equation:

$$\nabla^2 c = 0 \quad [3]$$

Dirichlet (fixed concentration) boundary conditions are applied to opposite ends of the REV. For simplicity, the values 0 and 1 are used

for an REV of dimension L:

$$c_{z=0} = 0 \quad [4]$$

$$c_{z=L} = 1 \quad [5]$$

Since we only solve Equation 2 in one of the phases, no electrochemical reaction or transport is assumed to occur at the solid-liquid interface. Therefore, the interface is modeled as an insulated wall. From the computed steady-state solution, the effective diffusivity and conductivity can be obtained by numerically integrating the concentration gradient over an arbitrary cross-section in the normal direction. For $L = 1$, this becomes

$$D^* \equiv \frac{\sigma^{\text{eff}}}{\sigma^{\text{bulk}}} = \frac{\kappa^{\text{eff}}}{\kappa^{\text{bulk}}} = \frac{D_2^{\text{eff}}}{D_2^{\text{bulk}}} = \int_A \nabla c \cdot \vec{n} dA|_z \quad [6]$$

In addition to the effective diffusivity and conductivity in the electrodes, the interfacial electrochemical reaction rate is another quantity with a homogenized treatment based on an idealized spherical particle in the macroscopic model. The corresponding microscopic simulations begin by simultaneously solving a set of four transport equations, one for each state variable (ion concentration c and electric potential φ) and in each phase (subscript 1 for solid and 2 for liquid):

$$\nabla \cdot (\sigma \nabla \varphi_1) = 0 \quad [7]$$

$$\nabla \cdot \left(-\kappa \nabla \varphi_2 - \frac{\kappa RT}{F} \left(1 + \frac{\partial \ln f}{\partial \ln c_2} \right) (1 - t_+^0) \nabla \ln c_2 \right) = 0 \quad [8]$$

$$\nabla \cdot (-D_1 \nabla c_1) = 0 \quad [9]$$

$$\nabla \cdot (-D_2 \nabla c_2) + \frac{\vec{i}_2 \cdot \nabla t_+^0}{F} = 0 \quad [10]$$

Again, Dirichlet boundary conditions are applied at opposite ends of the REV for all four state equations. The boundary conditions are linearized based on the local concentration $c_{1,i}$ and its spatial gradient in the axial direction:

$$c_{1,z=0} = c_{1,i} - \frac{L}{2} \frac{\partial c_{1,i}}{\partial x} \quad [11]$$

$$c_{1,z=L} = c_{1,i} + \frac{L}{2} \frac{\partial c_{1,i}}{\partial x} \quad [12]$$

Analogous forms of the boundary conditions are used for the other state variables c_2, φ_1, and φ_2. To generate simulation data for constructing surrogate models, the boundary conditions in Equations 11 and 12 are selected using a design of experiments for the state variables; in the completed multi-scale model, they are defined by the instantaneous, localized state variables from the macroscopic scale. As in the effective transport simulations, the solid-liquid interface is modeled as an insulated wall, effectively decoupling the governing equations in the two phases. Finally, the solution of Equations 7-10 is used to calculate the localized electrochemical reaction flux j_{flux} along the interface based on Butler–Volmer kinetics:

$$j_{\text{flux}} = k c_2^{0.5} (c_t - c_1)^{0.5} c_1^{0.5} \text{BV}(\eta) \quad [13]$$

$$\text{BV}(\eta) = \left(\exp\left(\frac{F}{2RT} \eta \right) - \exp\left(-\frac{F}{2RT} \eta \right) \right) \quad [14]$$

where overpotential η is defined as the difference between the local electric potential drop between the two phases, and the local open-circuit potential U_{ocp}:

$$\eta = \varphi_1 - \varphi_2 - U_{ocp}(c_1) \quad [15]$$

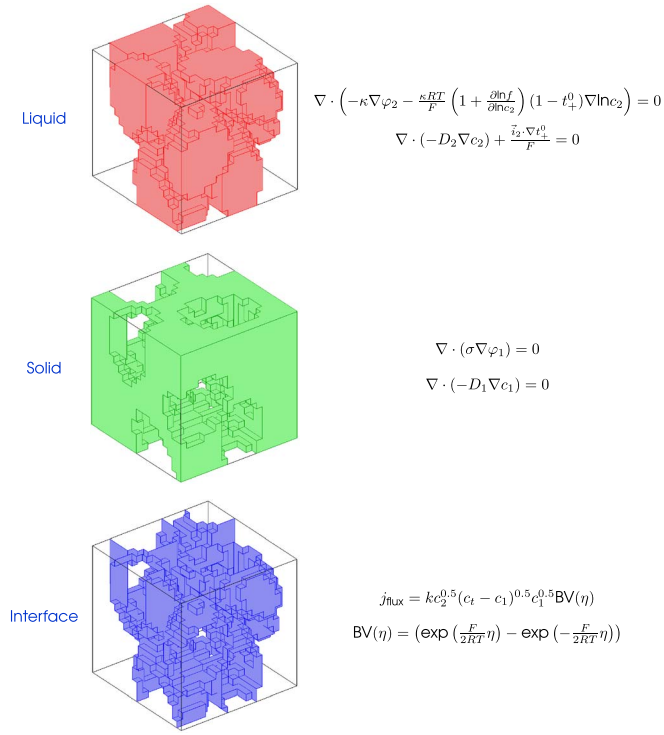

Figure 4. Summary of governing equations in solid and liquid phase for sample REV realization with 10 particles.

Finally, the overall reaction current density is obtained by numerically integrating the flux over the entire interface, and normalizing by the total interfacial surface area:

$$J = \frac{F}{V} \int_{A_s} (D_1 \nabla c_1) \cdot \vec{n} dA = \frac{F}{V} \sum_{\Delta A} j_{\text{flux}} \Delta A \quad [16]$$

Note that all governing equations are steady state, and thus these simulations represent a quasi-steady analysis. This quasi-steady simplification is necessary to allow for a large number of REV realizations at a reasonable computational cost, and is justified given the relative length scales between the macroscopic and microscopic domains. Since diffusion and conduction occur over a much smaller distance in the REV than in the electrode, the transient effects can be reasonably ignored for multi-scale simulations at low to moderate cycling rates. Given that the macroscopic length scale is about ten times larger than the microscopic scale, the equivalent characteristic time scale for diffusion and conduction in the microscopic domain is achieved at one-tenth the cycling rate as that at the macroscopic scale, where we consider a rate of C/10 to be close to steady-state. Therefore, the maximum cycling rate under which the quasi-steady assumption holds is about 1C. The electrochemical kinetics are assumed to occur faster than diffusion and conduction, and thus they are also subject to the quasi-steady formulation. This assumption also implies that we ignore the formation of surface film and other mechanisms that may influence electrochemical kinetics. Also note that the same justification based on relative length scales can be made for the linearization of the boundary conditions. Compared to transient analysis, quasi-steady analysis provides a significant reduction in computational expense, as well as an improvement in numerical stability and robustness, two important considerations when executing a large number of simulations. Figure 4 illustrates the two phases and interface for a sample REV realization, and the corresponding governing equations in each phase. MATLAB is used as an interface for setting up the simulations, which are them performed in COMSOL Multiphysics, a commercial FEM software platform.

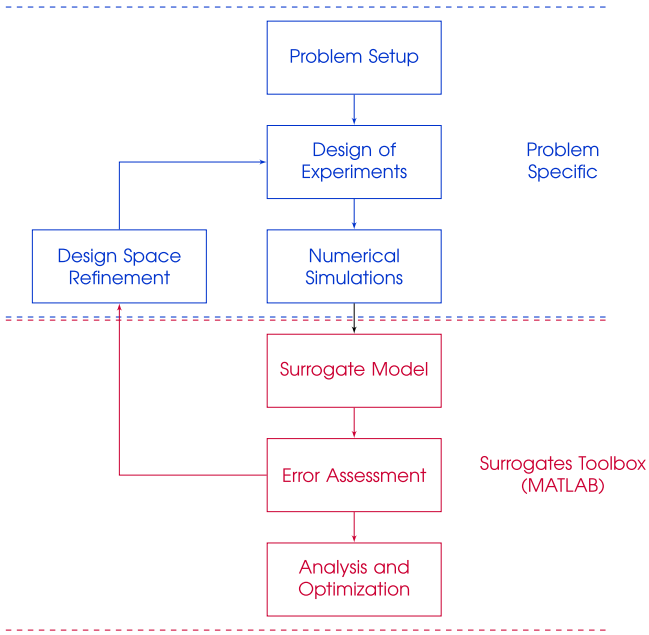

Figure 5. Procedure for surrogate-based modeling and analysis.

Surrogate modeling.— It is insufficient to merely compute transport and electrochemical properties for a large number of sample microstructures. To construct a multi-scale model for predicting the performance of a lithium-ion cell, a systematic method for efficiently incorporating the simulation data into existing cell-level (macroscopic) models is also required. Surrogate modeling, also known as response surface modeling or metamodeling, is a suitable method for bridging the gap between the macroscopic and microscopic length scales. A surrogate model is an approximation of the function being modeled ("surrogate function"), and is constructed using simulation data ("training data") acquired from a design of experiments.[36] It can be considered a generalized method for curve fitting in a multidimensional parameter space.[37] Engineering applications of surrogate modeling include the study of cativating fluid flow,[38] aircraft design,[39] value-based optimization,[40] stress in battery particles,[41] and design of battery electrodes.[42,43] In this section, we summarize the major components of the surrogate modeling methodology, focusing on the areas most relevant to the multi-scale model formulation.

As shown in Figure 5, the first step of the process is to create a design of experiments for the selected design or parameter space. Here, we employ a combined Latin Hypercube Sampling (LHS) and two-level face-centered composite design (FCCD) method. The FCCD method is useful for sampling the faces and vertices of the parameter space, while the LHS method efficiently fills the interior using stochastic stratified sampling.[44]

A set of simulations is then performed based on the design of experiments, and a surrogate function $\hat{y}$ is used to approximate the true function y for a vector of variables x. Two methods for accomplishing this are considered: polynomial response surface (PRS) and kriging. A PRS approximates the function as a combination of polynomial basis functions:

$$\hat{y}(\mathbf{x}) = \sum_i b_i f_i(\mathbf{x}) \qquad [17]$$

where the coefficients b_i are computed using a least-squares regression technique.

In contrast to PRS models, kriging models interpolate between training data points that the model fits exactly, by introducing an additional set of correlation basis functions[45] that act as a systematic departure $Z(\mathbf{x})$:

$$\hat{y}(\mathbf{x}) = \sum_i b_i f_i(\mathbf{x}) + Z(\mathbf{x}) \qquad [18]$$

The systematic departure components are assumed to be correlated as a function of the distance between the locations under consideration, and the maximum likelihood estimation is used to determine the parameter estimates.[46] The DACE toolbox used to construct and evaluate surrogate models in this study includes a variety of correlation function classes;[47] Gaussian correlation functions are generally found to offer the best accuracy for the microscopic simulation data and are selected for the global sensitivity analysis.

Once a surrogate model has been constructed, it is important to assess its accuracy by computing some error estimates. This is necessary for evaluating the suitability of applying the surrogate model for further analysis, for determining if domain refinement is required, and for comparing multiple surrogate models. Various procedures for error assessment have been proposed.[48] In this study we consider three error measures: the standard and adjusted coefficient of determination and (R^2 and R^2_{adj} respectively), and the prediction error sum of squares (PRESS). The coefficients of determination are computed directly from the training data:

$$R^2 = 1 - \frac{\sum_{i=1}^{N_s}(y(\mathbf{x}_i) - \hat{y}(\mathbf{x}_i))^2}{\sum_{i=1}^{N_s}(y(\mathbf{x}_i) - \bar{y})^2} \qquad [19]$$

$$R^2_{adj} = 1 - R^2 \frac{N_s - 1}{N_s - N_\beta} \qquad [20]$$

Note that both R^2 and R^2_{adj} are always less than or equal to 1, and that the equality condition is met when the surrogate approximation $\hat{y}$ matches the true function value y exactly for all sampling points $\mathbf{x}$. Thus, a value closer to 1 indicates a more accurate surrogate model. Also note that R^2_{adj} includes a dependency on the number of sampling points N_s, and is always less than R^2 when the number of degrees of freedom N_β exceeds 1. The other error measure, PRESS, is defined as the sum of the "leave-one-out" prediction errors at all training data points. This is the special $k = 1$ case of the more general "leave-k-out" approach, where larger values of k are suitable for problems with large N_s.[49] PRESS is computed by evaluating the prediction error at a single point using a surrogate model constructed from all other data points, and repeating this procedure over the entire data set:

$$\text{PRESS} = \sqrt{\frac{1}{N_s}\sum_{i=1}^{N^s}\left(y_i - \hat{y}_i^{(-i)}\right)^2} \qquad [21]$$

One particularly useful application of surrogate modeling is global sensitivity analysis (GSA), which quantifies the relative sensitivity of a function to its various input variables.[50] GSA is valuable for problems involving many variables, as it can be used to reduce the problem size by identifying variables with little impact. This has been demonstrated for lithium-ion cell analysis using macroscopic models,[31,42] and is also highly relevant for multi-scale model development. Although GSA can be performed without a surrogate model, the surrogate model can be evaluated much more quickly than the true objective function, since surrogate functions are analytically defined. This improvement in computational efficiency allows GSA results to be computed much faster, since the number of function evaluations required for GSA scales exponentially with the number of variables.[48] Here, we compute sensitivity estimates using Sobol's method of linear decomposition.[51] Further details of the GSA methodology are provided in Appendix B.

Results and Discussion

Effective transport coefficients.— Using the automated simulation procedure outlined in Figure 2, a total of 2462 REV realization cases are simulated, which includes 2300 with 10 particles (10 μm), 130

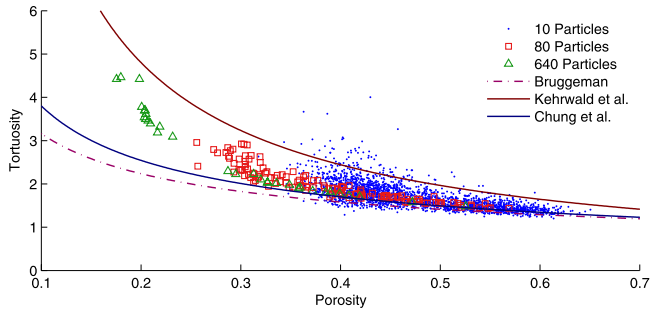

Figure 6. Comparison of porosity-tortuosity results for 2462 REV realizations with Bruggeman equation and experiments.

with 80 particles (20 μm), and 32 with 640 particles (40 μm). This number of realizations is selected to balance the available computational resources with the need for a large data set to ensure statistically meaningful results. To compare the results to the Bruggeman equation used in the macroscopic model, as well as experimental results in the literature, the tortuosity τ is calculated from the effective diffusivity D^* and porosity ε:

$$\frac{1}{D^*} = \frac{D^{\text{bulk}}}{D^{\text{eff}}} = \frac{\tau}{\varepsilon} \quad [22]$$

This equation is commonly used to study porosity and tortuosity, in both experimental and numerical studies.[52]

Figure 6 compares the porosity-tortuosity relationship in the computed results with the Bruggeman equation ($\tau = \varepsilon^{-0.5}$) and two proposed corrections based on experimental measurements by Kehrwald et al.[21] ($\tau = \varepsilon^{-0.975}$) and simulations by Chung et al.[53] ($\tau = \varepsilon^{-0.58}$ for inhomogeneous spherical particles). The Bruggeman equation underpredicts the tortuosity, and thus overpredicts the effective diffusivity and conductivity. The difference between the simulation results and the Bruggeman equation also becomes greater at low porosity, where the tortuosity is greatest. This confirms that the Bruggeman equation tends to overpredict the cell performance when implemented in the macroscopic model. Although the majority of the REV realizations fall in a higher porosity range than the experimental samples, good agreement in tortuosity is found between simulations and experiments at common porosity levels. There is also good agreement in the porosity-tortuosity relationship between the 80 particle and 640 particle cases, suggesting domain size independence beyond 80 particles. The microscopic simulation results generally fall between those from the two aforementioned references; the differences suggest that particle shape and size distribution, two factors not considered in the present model, may significantly influence transport within porous electrodes.

The same simulation results are plotted as effective diffusivity against porosity in Figure 7. A proposed value of $\alpha = 1.681$ is shown to be able to model the normalized diffusivity with a coefficient of determination of $R^2 = 0.894$.

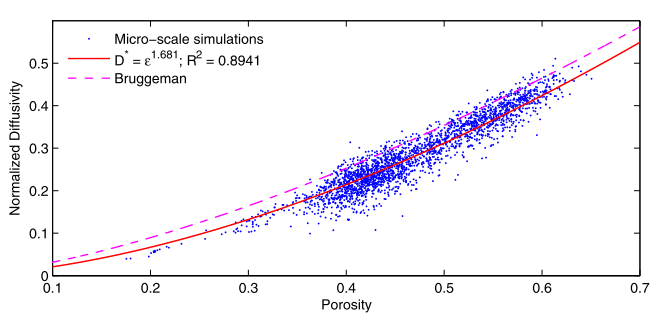

Figure 7. Diffusivity-porosity results for 2462 REV realizations with proposed transport model and Bruggeman equation.

Table I. Ranges of variables used in design of experiments for surrogate modeling of reaction current density.

Parameter	Minimum	Maximum
c_1	4.7×10^3 mol/m^3	2.1×10^4 mol/m^3
c_2	600 mol/m3	1000 mol/m^3
φ_1	3.0 V	4.15 V
φ_2	−1.0 V	0
$\frac{\partial c_1}{\partial x}$	-8.2×10^7 mol/m^4	0
$\frac{\partial c_2}{\partial x}$	-6.5×10^6 mol/m^4	0
$\frac{\partial \varphi_1}{\partial x}$	−40 V/m	0
$\frac{\partial \varphi_2}{\partial x}$	−550 V/m	0

Although this value is lower than is typical in surrogate modeling studies, significant variation can be expected due to the random nature of the microstructure generation and relatively small number of particles in each REV. Note that a power law of the same form as the Bruggeman equation is selected instead of a polynomial or any other class of function, as it satisfies two important boundary conditions:

$$D^*_{\varepsilon=1} = \frac{D^{\text{eff}}_{\varepsilon=1}}{D^{\text{bulk}}} = 1 \quad [23]$$

$$D^*_{\varepsilon=0} = 0 \quad [24]$$

These two boundary conditions ensure that the results match the bulk properties of the material, and that no transport occurs when no material is available. It is important to note that although the effective diffusivity and conductivity can vary considerably for a given porosity level due to the orientation and positioning of the particles, these fluctuations are dissipated over the larger domain of an entire electrode. The statistical averaging of a large number of REV realizations, and the relative length scales between the macroscopic and microscopic models, allow porosity effects to outweigh local anomalies in microstructure, and thus this modified treatment of effective transport coefficients is independent of the cycling rate.

Interfacial electrochemical kinetics.— Recall that the local ion concentration and electric potential, and their spatial derivatives, are required as boundary conditions for the two-phase microscopic simulations. To properly map the output of the microscopic simulations (the local reaction current density) to the macroscopic state variables, the surrogate model must account for all four state variables and their derivatives as inputs. We use a design of experiments that models these state variables as independent input parameters to ensure that the surrogate model accounts for the entire parameter space within the electrode during cell operation. The corresponding ranges considered in the design of experiments are summarized in Table I.

This 8-parameter space is again populated with a combined FCCD and LHS approach. An additional constraint on the overpotential η is applied as a filter:

$$-0.1 \leq \eta \leq 0 \quad [25]$$

This constraint is necessary to ensure that the exponential terms in the Butler–Volmer equation do not become unbounded. As shown in Figure 8, this constraint is not particularly restrictive as it significantly exceeds the operational space within the cathode for a sample discharge cycle at 16 A/m^2 (equivalent to 1C). The constraint also serves the secondary purpose of reducing the number of sample simulations required to train the surrogate model, and concentrating more data points within the relevant part of the parameter space.

A total of 635 sampling points are selected in this design of experiments; this same set of simulations is applied to each REV realization. As in the effective transport simulations, differences in microstructure can cause significant deviation in the results, so an averaging of a statistically meaningful number of realizations is necessary. However, since 635 simulations must be applied to each

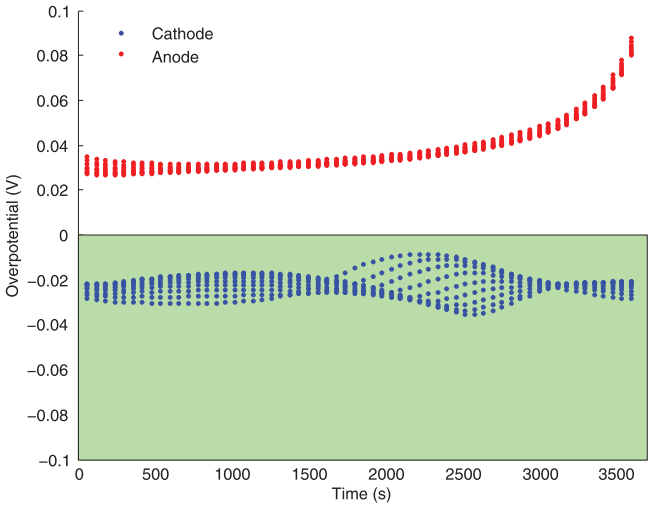

Figure 8. Overpotential distribution within anode and cathode during a sample 16 A/m^2 cell discharge; constraint space is highlighted in green.

realization, and since four transport equations must be solved simultaneously, the number of REV that can be considered at a reasonable computational cost is much smaller. The surrogate model is trained using data obtained from the averaging of 18 REV realizations with porosity between 0.3995 and 0.4005 (although simulations at other porosity levels are considered for GSA in the following section). This narrow range is selected to facilitate comparisons between the macroscopic and microscopic models. A sample result for one REV realization at one point in the design of experiments is shown in Figure 9.

A procedure for comparing the length scales is described as follows. A single cell discharge cycle (in this case, at a rate of 1C = 16 A/m^2) is performed using the macroscopic homogeneous model, and the reaction current density distribution within the cathode is computed at specified time steps, in addition to the solution for all other relevant state variables (local Li^+ ion concentration and electric potential in both phases, and their spatial derivatives). A set of microscopic simulations is then applied to 18 REV realizations using the macroscopic state variables as boundary conditions, and the interfacial reaction current density is computed at each sample in time and space. Figure 10 compares the averaged results from the 18 realizations with those from the macroscopic mode, at three locations within the cathode for every 60 seconds in a 3600-second cell discharge.

A clear difference can be observed between the results from the two length scales, with the microscopic simulations generally exhibiting greater variation than the homogenized equation. Note that the total reaction current integrated over space and time are not equal, because the microscopic simulations are sampled independently of one another, and the coupling with the cell model is unidirectional. The interfacial surface area is also different, as the homogenized equation is based on the surface area of an idealized sphere, whereas the microscopic simulations use the area between the solid and liquid phases. As a result, it appears that the total charge in the electrode is not conserved; however, this issue is resolved when the bidirectional coupling of length scales is completed in the multi-scale model.

Surrogate-based coupling of models.— Since the surrogate model is used to bridge the scales in the multi-scale model, it is important to assess the performance of the surrogate model. A kriging surrogate is found to have the lowest normalized PRESS value of 7.5%, a value that is sufficiently high that the microstructure information is likely to be lost due to uncertainty in the surrogate. We thus apply GSA to reduce the dimensionality of the surrogate.

The main and total sensitivity indexes are calculated by applying Sobol's method to the kriging model, and are plotted in Figure 11. It

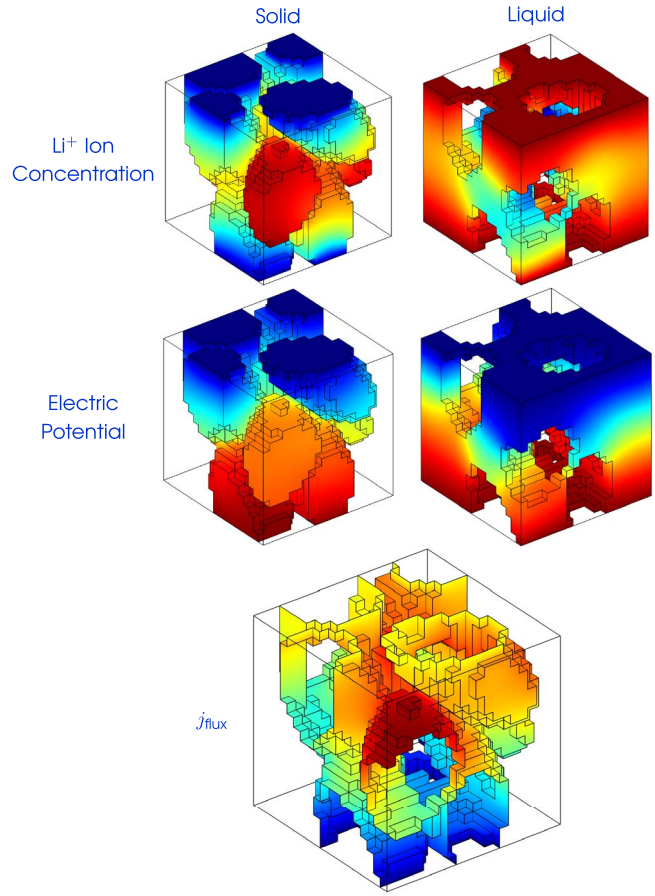

Figure 9. Sample simulation result for 10-particle case; colors represent ion concentration and electric potential relative to maximum (red) and minimum (blue) in Table I.

is immediately apparent that the variation in reaction current density is dominated by the magnitude of the two-phase electric potentials φ_1 and φ_2, and the solid-phase ion concentration c_1. The dominant effect of the electric potentials can be explained by the functional form of the Butler–Volmer equation, in which the overpotential is embedded in the exponential terms, while the ion concentration appears in the polynomial terms. Note that all four gradient terms are

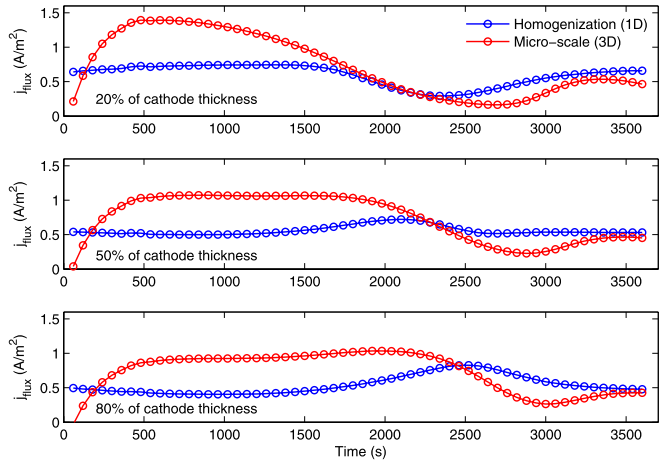

Figure 10. Comparison of local reaction current density at 20% (top), 50% (middle) and 80% (bottom) of cathode thickness, computed using macroscopic (homogenized Butler-Volmer kinetics) and microscopic (3D simulations) models.

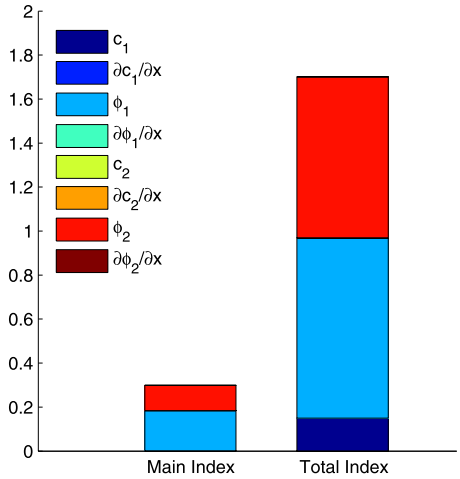

Figure 11. Sensitivity indexes calculated from kriging surrogate for reaction current density (8 input variables).

found to have negligible impact, a result that can be explained by the bounds in Table I, and by the application of boundary conditions in Equations 11 and 12. The magnitude of the difference between the boundary conditions tends to be much lower than the mean value within the REV, which has dimension $L = 10 \times 10^{-6} = 10^{-5}$ m. For example, the variation in c_1 across the REV due to the spatial gradient is at most $8.2 \times 10^7 \times 10^{-5} = 8.2 \times 10^2 \text{mol/m}^3$, which is 5% of the c_1 range considered in the design of experiments.

The global sensitivity indexes allow the surrogate model to be reduced from 8 to 3 input variables, while simultaneously improving the accuracy of the surrogate model by reducing the PRESS value from 7.5% to 3.9%. The accuracy of the surrogate model can be assessed by using it to evaluate the reaction current density at the same points as in Figure 10, and the results are plotted in Figure 12 along with the micro-simulation data used to train the surrogate.

The surrogate model matches the microscopic simulations very well until about $t = 3100$ s, at which point the models start to sharply deviate at all locations within the electrode. The reason for this deviation is unclear, although it is likely due to one of the spatial gradients being sampled outside the well defined parameter space. Since numerical robustness is of critical importance in developing a multi-scale model suitable for design optimization, the kriging model is insufficient despite its good accuracy prior to failing. Another limitation of the kriging surrogate is that while it is a smooth function, its gradients

Table II. Coefficients of 4th-order PRS for reaction current density.

$k_{0,0}$	10.4	$k_{1,0}$	−87.4	$k_{2,1}$	478
$k_{0,1}$	89.4	$k_{1,1}$	−298	$k_{2,2}$	580
$k_{0,2}$	14.9	$k_{1,2}$	697	$k_{3,0}$	−316
$k_{0,3}$	28656	$k_{1,3}$	364	$k_{3,1}$	271
$k_{0,4}$	16256	$k_{2,0}$	257	$k_{4,0}$	139

are not explicitly defined. Therefore, efficient solvers that require gradients have significant difficulty converging to a solution due to poor accuracy in gradient estimation. This problem has been documented for a multi-scale model using non-smooth functions to couple the length scales.[30] For these reasons, a PRS surrogate is selected instead, since it has explicitly defined smooth gradients.

To construct the PRS, we note that the parameter space can be further reduced by combining the two electric potentials φ_1 and φ_2 into a single input to the surrogate as the overpotential η. A PRS function of order N for $\hat{j}_{\text{flux}}$ with respect to two input variables c_1 and η can be written as a summation of basis functions:

$$\hat{j}_{\text{flux}} = \sum_{i=0}^{N} \sum_{j=0}^{N} k_{i,j} c^i \eta^j \quad [26]$$

$$k_{i,j} = 0 \text{ if } i + j > N \quad [27]$$

where the coefficients $k_{i,j}$ are determined using a least-squares regression method for $i + j \leq N$. A fourth-order model ($N = 4$) is found to have a coefficient of determination of $R^2 = 0.948$, and the corrresponding coefficients are listed in Table II.

Although higher order PRS fits are possible, the number of polynomial terms increases dramatically, making the definition of analytical derivatives a tedious process. An assessment of the surrogate model accuracy can again be made by comparing the local reaction current density profiles with those computed using the surrogate.

As shown in Figure 13, some differences between the surrogate model and the microscopic simulation data can be observed, especially in the early part of the discharge. However, the surrogate matches the microscopic simulations much more closely toward the end of the discharge, when the macroscopic and microscopic models diverge considerably. This means that the surrogate model successfully bridges the microscopic simulation data into the multi-scale model, despite some of the microstructural information being lost due to limitations in the surrogate model. Refinement of the parameter space to improve the accuracy of the surrogate model would enhance the value of the multi-scale model for cell-level analysis and optimization.

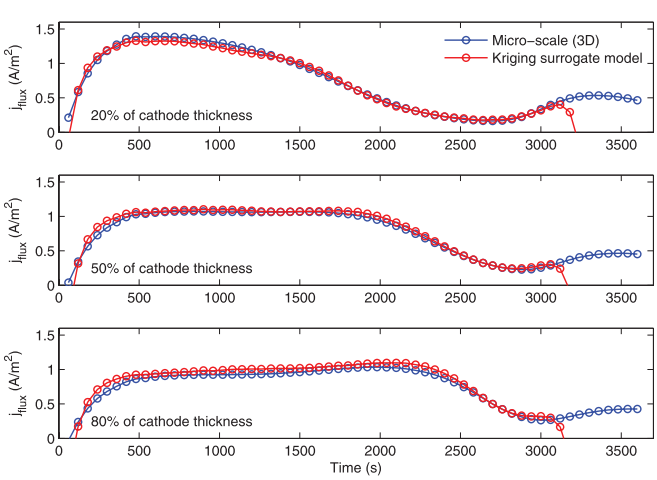

Figure 12. Comparison of local reaction current density computed using microscopic simulations and kriging surrogate (3 input variables).

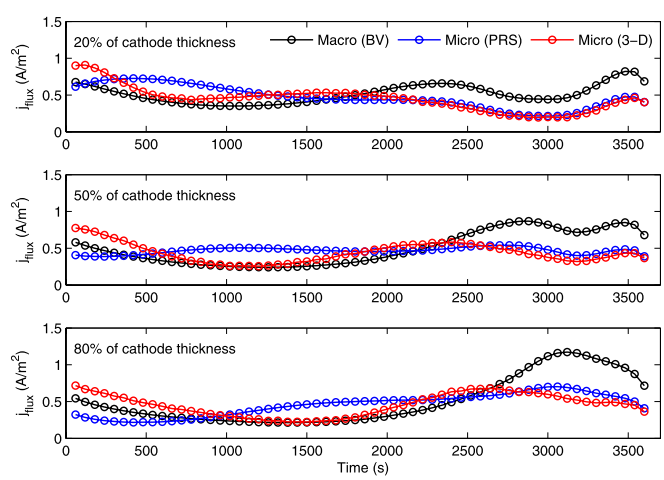

Figure 13. Comparison of local reaction current density computed using microscopic simulations and PRS surrogate (2 input variables).

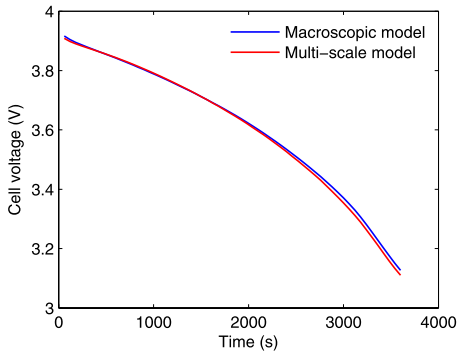

Figure 14. Cell voltage comparison of macroscopic and multi-scale models for a single 16 A/m^2 discharge.

Finally, the multi-scale model is compared to the macroscopic model at the cell level by plotting the cell voltage profiles for a single discharge simulation. As shown in Figure 14, the two models produce very similar results, with the multi-scale model giving a slightly lower cell voltage due to the reduction in effective diffusivity and conductivity. This similarity indicates that the cell level performance depends much more on the total amount of ions and electrons being transported than their distribution within the electrodes. Comparable results are also observed when the discharge rate is adjusted. The similarity of the macroscopic and multi-scale simulation results may call into question the value of developing the multi-scale model. However, it is important to note that this had not been established prior to completing the multi-scale model and obtaining the results. Therefore, the documentation of the comparison between the macroscopic, microscopic and surrogate models, and the quantification of the impact of such differences on the cell level performance, provide meaningful insights into the relevant physics of the system. Furthermore, it is known that some important phenomena, such as phase transition that causes dissolution of active solid in the electrolyte[54] and capacity fade due to growth of the solid-electrolyte interface (SEI),[55] are strongly dependent on local conditions within the electrode. Since the present multi-scale model does not consider these mechanisms, their influence on cell performance cannot be assessed. Fortunately, the surrogate modeling framework employed here can be readily extended to incorporate additional microscopic models for these degradation mechanisms into the multi-scale model, which would greatly expand the benefit of applying the multi-scale model to cell and battery design.

Conclusions

In this section, we summarize the most significant contributions of this work. First, we have successfully established a multi-scale model that utilizes data from physics-based microscopic 3D models while retaining the computational efficiency of existing macroscopic homogeneous models. Second, the microscopic simulation data provide valuable insights into the physical phenomena that govern diffusion, conduction, and electrochemical kinetics within electrode particles. Third, we have demonstrated a general computational framework for studying engineering problems at multiple scales using the surrogate modeling methodology.

In the microscopic simulations, the effective ion diffusivity and electronic conductivity in the porous cathode are related to their bulk values, and the local interfacial reaction current density is modeled by applying Butler–Volmer electrochemical kinetics locally to the computed ion concentration and electric potential distributions in the two phases. The electrode microstructure is simulated by randomly packing ellipsoidal particles to create REV realizations, and a robust voxel method is employed for meshing. From the effective transport simulation results, a modification to the Bruggeman equation ($\alpha = 1.68$) is established based on computed porosity-tortuosity relationships and incorporated into the multi-scale model. This is accomplished by generating a statistically significant number of REV realizations and averaging the results. The Bruggeman equation used in homogenized models is found to consistently underpredict tortuosity in the porous medium, and thus overpredict diffusivity and conductivity. This can pose an important problem for batteries designed using simplified models, in which the overpredictions in diffusivity and conductivity lead to overpredictions in energy and power performance.

To model electrochemical kinetics, a PRS surrogate model with respect to two variables (solid-phase ion concentration c_1 and overpotential η) is selected as the coupling mechanism for bridging the length scales to complete the multi-scale model. This method takes advantage of the superior robustness and analytically defined gradients of the PRS model, to avoid the added computational cost of explicitly coupling the governing equations of the macroscopic and microscopic models. The reaction current density is modeled as a quasi-steady solution of diffusion and conduction in the solid and liquid phases with Butler–Volmer kinetics at the interface. The number of input variables to the PRS is reduced using GSA results with a kriging model.

It is important to note some promising directions for future efforts. As previously discussed, the present multi-scale model does not include degradation mechanisms and thus provides an incomplete picture of the impact of microstructure oncell performance. The inclusion of validated models for phase transition and SEI growth in future iterations of the model is of critical importance since cycle life is a principal concern in the design of batteries for high-power applications such as electric vehicles. It is also important that a multi-scale treatment be extended in both electrodes, since important processes such as capacity fade are known to occur in the anode.[56] Another goal would be to apply the established multi-scale model to assess the impact of varying the microstructure on the cell-level performance, especially since only a narrow porosity range is sampled for the electrochemical kinetics simulations.

The surrogate modeling methodology is a well suited numerical tool for realizing these objectives, each of which represents a major step toward achieving higher performance batteries using high-fidelity, efficient computational models. Finally, the present microscopic modeling methodology aims to generate realistic microstructures without any attempt to tailor the microstructure for directional diffusion or interfacial surface area. Recent advances in the design of piezoelectric ceramic microstructures hold significant promise if similar techniques can be extended to battery electrode materials.[57] The development of accurate modeling capabilities for arbitrary classes of microstructures (including those with polydisperse or non-ellipsoidal particles) would represent another critical step toward designing new high-capacity materials capable of further improving energy and power density.

Acknowledgment

This work was supported by the General Motors and University of Michigan Advanced Battery Coalition for Drivetrains (ABCD).

Appendix A

Macroscopic Cell Model

The multi-scale uses a COMSOL Multiphysics implementation of the pseudo-2D model based on porous electrode theory.[14,15] It is called pseudo-2D because it models lithium ion and electric potential distributions along an axial dimension across the thickness of the cell, while accounting for the effect of particle size by applying the superposition principle to introduce a radial pseudo-dimension at each computational node to compute the rate of ion diffusion within a spherical pseudo-particle. Along the axial dimension, the electric potential distribution in the solid and liquid phases is modeled using steady transport equations:

$$\nabla \cdot (\sigma^{\text{eff}} \nabla \varphi_1) - J = 0 \qquad [A1]$$

$$\nabla \cdot \left(\kappa^{\text{eff}} \nabla \varphi_2\right) + \nabla \cdot (\kappa_D \nabla (\ln c_2)) + J = 0 \qquad [A2]$$

The axial dimension also models transient lithium ion diffusion in the liquid phase:

$$\varepsilon_2 \frac{\partial c_2}{\partial t} = \nabla \cdot (D_2^{\text{eff}} \nabla c_2) + \frac{1 - t_+^0}{F} \nabla \cdot \vec{i}_2 - \frac{\vec{i}_2 \cdot \nabla t_+^0}{F} \quad [A3]$$

At the interfaces between electrodes and current collectors, fixed boundary conditions are applied:

$$\nabla \varphi_1 = \frac{-I_{dis}}{\sigma} \quad [A4]$$

$$\sigma \nabla \varphi_2 = 0 \quad [A5]$$

$$\nabla c_2 = 0 \quad [A6]$$

Note that all three equations in the axial dimension involve an effective transport coefficient, which is calculated from bulk properties using the Bruggeman equation 1. The second radial dimension models the time-dependent ion concentration distribution within spherical particles:

$$\frac{\partial c_1}{\partial t} = \frac{1}{r^2} \frac{\partial}{\partial r} \left(D_1 r^2 \frac{\partial c_1}{\partial r} \right) \quad [A7]$$

Boundary conditions for the temporal and spatial dimensions are applied at the center and surface of the sphere, respectively:

$$\frac{\partial c_1}{\partial t}_{r=0} = 0 \quad [A8]$$

$$-D_1 \frac{\partial c_1}{\partial t}_{r=R_1} = \frac{i_n}{F} \quad [A9]$$

The solid and liquid phases are coupled via the Butler–Volmer equation, applied to the the surface area a_1:

$$J = a_1 i_0 \left(\exp\left(\frac{F}{2RT} \eta \right) - \exp\left(-\frac{F}{2RT} \eta \right) \right) \quad [A10]$$

$$a_1 = \frac{3\varepsilon_1}{R_1} \quad [A11]$$

Appendix B

Global Sensitivity Analysis

GSA is a method for quantifying the relative sensitivity of a function to each of its input variables, which can provide useful insights into the nature of the parameter space and allow the problem size to be reduced by identifying variables with little impact. Global sensitivity indexes are computed using Sobol's method.[51] The surrogate function f can be decomposed as a linear combination of functions of subspaces of the parameter space, also known as additive functions:

$$f(\vec{x}) = f_0 + \sum_i f_i(x_i) + \sum_{i<j} f_{ij}(x_i, x_j) + \ldots + f_{1\ldots N_v}(x_1, \ldots, x_{N_v}) \quad [B1]$$

where N_v is the number of input variables in $\vec{x}$. The total variance $V(f)$ is defined as the expected value of the square of the summation of all non-zero order additive functions, and can also be expressed as a sum of partial variances of individual variables and combinations of variables:

$$V(f) = \sum_{i=1}^{N_v} V_i + \sum_{i<j} V_{ij} + \ldots + V_{1\ldots N_v} \quad [B2]$$

The partial variances are in turn defined in terms of the expected value of the additive functions:

$$\begin{aligned} V_i &= V(E(f|x_i)) \\ V_{ij} &= V(E(f|x_i, x_j)) - V_i - V_j \\ &\ldots \end{aligned} \quad [B3]$$

The expected values E of the additive functions and their variances can be expressed as integrals of the additive functions:

$$E(f|x_i)_i = \int_0^1 f_x dx_i \quad [B4]$$

$$V(E(f|x_i)) = \int_0^1 f_x^2 dx_i \quad [B5]$$

These integrals are estimated using various numerical approximations; we use a five-point Gauss quadrature scheme. The partial variances can then be used to compute main and total sensitivity indexes:

$$S_{M,i} = \frac{V_i}{V(f)} \quad [B6]$$

$$S_{T,i} = S_{M,i} + \frac{\sum_{j \neq i} V_{ij}}{V(f)} \quad [B7]$$

Note that the main index $S_{M,i}$ and total index $S_{T,i}$ are always normalized between 0 and 1, and that $S_{T,i} \geq S_{M,i}$. The difference between the two is the effect of cross-terms between multiple variables.

References

1. M. Armand and J.-M. Tarascon, *Nature*, **451**, 652 (2008).
2. V. Ramadesigan, R. N. Methekar, F. Latinwo, R. D. Braatz, and V. R. Subramanian, *J. Electrochem. Soc.*, **157**, A1328 (2010).
3. S. De, P. W. C. Northrop, V. Ramadesigan, and V. R. Subramanian, *J. Power Sources*, **227**, 161 (2012).
4. N. Xue, W. Du, A. Gupta, W. Shyy, A. M. Sastry, and J. R. R. A. Martins, *J. Electrochem. Soc.*, **160**, A1071 (2013).
5. S. Golmon, K. Maute, and M. L. Dunn, *J. Power Sources*, **253**, 239 (2014).
6. X. Zhang, W. Shyy, and A. M. Sastry, *J. Electrochem. Soc.*, **154**, A910 (2007).
7. W. Luo, C. Lyu, L. Wang, and L. Zhang, *J. Power Sources*, **241**, 295 (2013).
8. P. Ramadass, B. Haran, R. White, and B. N. Popov, *J. Power Sources*, **123**, 230 (2003).
9. R. E. Garcia, Y.-M. Chiang, W. C. Carter, P. Limthongkul, and C. M. Bishop, *J. Electrochem. Soc.*, **152**, A255 (2005).
10. C.-W. Wang and A. M. Sastry, *J. Electrochem. Soc.*, **154**, A1035 (2007).
11. B. Y. Liaw, G. Nagasubramanian, R. G. Jungst, and D. H. Doughty, *Solid State Ionics*, **175**, 835 (2004).
12. X. Hu, S. Li, and H. Peng, *J. Power Sources*, **198**, 359 (2012).
13. V. Ramadesigan, P. W. C. Northrop, S. De, D. Santhanagopalan, R. D. Braatz, and V. R. Subramanian, *J. Electrochem. Soc.*, **159**, R31 (2012).
14. T. F. Fuller, M. Doyle, and J. Newman, *J. Electrochem. Soc.*, **141**, 1 (1994).
15. M. Doyle, J. Newman, A. S. Gozdz, C. N. Schmutz, and J.-M. Tarascon, *J. Electrochem. Soc.*, **143**, 1890 (1996).
16. Y. Dai, L. Cai, and R. E. White, *J. Power Sources*, **247**, 365 (2014).
17. C. L. Cobb and M. Blanco, *J. Power Sources*, **249**, 357 (2014).
18. N. Xue, W. Du, T. A. Greszler, W. Shyy, and J. R. R. A. Martins, *Applied Energy*, **115**, 591 (2014).
19. V. Ramadesigan, V. Boovaragavan, J. C. Pirkle, and V. R. Subramanian, *J. Electrochem. Soc.*, **157**, A854 (2010).
20. P. W. C. Northrop, V. Ramadesigan, S. De, and V. R. Subramanian, *J. Electrochem. Soc.*, **158**, A1461 (2011).
21. D. Kehrwald, P. R. Shearing, N. P. Brandon, P. K. Sinha, and S. J. Harris, *J. Electrochem. Soc.*, **158**, A1393 (2011).
22. K. K. Patel, J. M. Paulsen, and J. Desilvestro, *J. Power Sources*, **122**, 144 (2003).
23. A. Vadakkepatt, B. L. Trembacki, S. R. Mathur, and J. Y. Murthy, in *ASME 2013 Heat Transfer Summer Conference collocated with the ASME 2013 7th International Conference on Energy Sustainability the ASME 2013 11th International Conference on Fuel Cell Science Engineering Technology*, p. V003T21A016–V003T21A016, American Society of Mechanical Engineers (2013).
24. A. Gupta, J. H. Seo, X. Zhang, W. Du, A. M. Sastry, and W. Shyy, *J. Electrochem. Soc.*, **158**, A487 (2011).
25. A. A. Franco, *RSC Adv.*, **3**, 13027 (2013).
26. A. Awarke, S. Lauer, M. Wittler, and S. Pischinger, *Comp. Mat. Sci.*, **50**, 871 (2011).
27. X. Xiao, W. Wu, and X. Huang, *J. Power Sources*, **195**, 7649 (2010).
28. S. Golmon, K. Maute, and M. L. Dunn, *Comp. & Struct.*, **87**, 1567 (2009).
29. S. Golmon, K. Maute, and M. L. Dunn, *Int. J. Num. Meth. Eng.*, **92**, 475 (2012).
30. W. Du, *PhD thesis*, University of Michigan (2013).
31. W. Du, N. Xue, A. M. Sastry, J. R. R. A. Martins, and W. Shyy, *J. Electrochem. Soc.*, **160**, A1187 (2013).
32. A. Donev, S. Torquato, and F. H. Stillinger, *J. Comp. Phys.*, **202**, 765 (2005).
33. A. Donev, S. Torquato, and F. H. Stillinger, *J. Comp. Phys.*, **202**, 737 (2005).
34. S. J. Hollister, J. M. Brennan, and N. Kikuchi, *J. Biomech.*, **27**, 433 (1994).
35. K. Koketsu, H. Fujiwara, and Y. Ikegami, *Pure and Applied Geophysics*, **161**, 2183 (2004).
36. D. C. Montgomery and R. H. Myers, *Response surface methodology: process and product optimization using designed experiments* (1995).
37. W. Shyy, Y.-C. Cho, W. Du, A. Gupta, C.-C. Tseng, and A. M. Sastry, *Acta Mech. Sinica*, **27**, 845 (2011).
38. C.-C. Tseng and W. Shyy, *Int. J. Heat and Mass Transfer*, **53**, 513 (2010).
39. R. P. Liem, C. A. Mader, E. Lee, and J. R. R. A. Martins, in *13th AIAA Aviation Technology Integration, Operations Conference* (2013).
40. R. Moore, D. A. Romero, and C. J. J. Paredis, in *Proceedings of ASME International Design Engineering Technical Conferences* (2011).
41. X. Zhang, A. M. Sastry, and W. Shyy, *J. Electrochem. Soc.*, **155**, A542 (2008).
42. W. Du, A. Gupta, X. Zhang, A. M. Sastry, and W. Shyy, *Int. J. Heat and Mass Transfer*, **53**, 3552 (2010).
43. W. Du, N. Xue, A. Gupta, A. M. Sastry, J. R. R. A. Martins, and W. Shyy, *Acta Mech. Sinica*, **29**, 335 (2013).
44. M. D. McKay, R. J. Beckman, and W. J. Conover, *Technometrics*, **21**, 239 (1979).
45. D. R. Jones, *J. Global Optim.*, **21**, 345 (2001).
46. J. Sacks, W. J. Welch, T. J. Mitchell, and H. P. Wynn, *Stat. Sci.*, **4**, 409 (1989).
47. S. N. Lophaven, H. B. Nielsen, and J. Sondergaard, Dace-a matlab kriging toolbox, version 2.0. Technical report (2002).
48. N. V. Queipo, R. T. Haftka, W. Shyy, T. Goel, R. Vaidyanathan, and K. P. Tucker, *Prog. in Aero. Sci.*, **41**, 1 (2005).

49. M. Meckesheimer, A. J. Booker, R. R. Barton, and T. W. Simpson, *AIAA J.*, **40**, 2053 (2002).
50. A. Saltelli, S. Tarantola, and K. P.-S. Chan, *Technometrics*, **41**, 39 (1999).
51. I. M. Sobol, *Math. Comp. Sim.*, **55**, 271 (2001).
52. B. Vijayaraghavan, D. R. Ely, Y.-M. Chiang, R. Garcia-Garcia, and R. E. Garcia, *J. Electrochem. Soc.*, **159**, A548 (2012).
53. D.-W. Chung, M. Ebner, D. R. Ely, V. Wood, and R. E. Garcia, *Model. Sim. Mat. Sci. Eng.*, **21**, 074009 (2013).
54. J. Vetter, P. Novak, M. R. Wagner, C. Veit, K.-C. Moller, J. O. Besenhard, M. Winter, M. Wohlfahrt-Mehrens, C. Vogler, and A. Hammouche, *J. Power Sources*, **147**, 269 (2005).
55. A. Awarke, S. Pischinger, and J. Ogrzewalla, *J. Electrochem. Soc.*, **160**, A172 (2013).
56. R. Spotnitz, *J. Power Sources*, **113**, 72 (2003).
57. S.-B. Lee, T. S. Key, Z. Liang, R. E. Garcia, S. Wang, X. Tricoche, G. S. Rohrer, Y. Saito, C. Ito, and T. Tani, *J. Euro. Ceramic Soc.*, **33**, 313 (2012).